

# Quantitative analyses of the plant cytoskeleton reveal underlying organizational principles

David Breuer<sup>1</sup>, Alexander Ivakov<sup>2</sup>, Arun Sampathkumar<sup>3</sup>, Florian Hollandt<sup>1</sup>, Staffan Persson<sup>2,4</sup>, Zoran Nikoloski<sup>1,\*</sup>

<sup>1</sup>*Systems Biology and Mathematical Modelling, Max Planck Institute of Molecular Plant Physiology,*

*Am Muehlenberg 1, 14476 Potsdam, Germany*

<sup>2</sup>*Plant Cell Walls, Max Planck Institute of Molecular Plant Physiology,*

*Am Muehlenberg 1, 14476 Potsdam, Germany*

<sup>3</sup>*Sainsbury Laboratory, University of Cambridge,*

*Bateman Street, Cambridge CB2 1LR, United Kingdom*

<sup>4</sup>*ARC Centre of Excellence in Plant Cell Walls, School of Botany, University of Melbourne,*

*Grattan Street, Parkville, Victoria 3010, Australia and*

*\*nikoloski@mpimp-golm.mpg.de*

The actin and microtubule cytoskeletons are vital structures for cell growth and development across all species. While individual molecular mechanisms underpinning actin and microtubule dynamics have been intensively studied, principles that govern the cytoskeleton organization remain largely unexplored. Here, we captured biologically relevant characteristics of the plant cytoskeleton through a network-driven imaging-based approach allowing to quantitatively assess dynamic features of the cytoskeleton. By introducing suitable null models, we demonstrate that the plant cytoskeletal networks exhibit properties required for efficient transport, namely, short average path lengths and high robustness. We further show that these advantageous features are maintained during temporal cytoskeletal re-arrangements. Interestingly, man-made transportation networks exhibit similar properties, suggesting general laws of network organization supporting diverse transport processes. The proposed network-driven analysis can be readily used to identify organizational principles of cytoskeletons in other organisms.

Keywords: cytoskeletal networks, cytoskeletal transport, plant cell walls, complex networks, organizational principles

## I. INTRODUCTION

Complex systems can be represented by networks that capture the underlying components, as nodes, and their interactions, as links. Network representations have provided insights into the organizational principles of a variety of systems, ranging from man-made to systems shaped by evolution, such as: metabolic networks [18, 36], neural networks [19, 40], food webs [38, 73], and transportation systems, including: vascular [22, 71] and leaf venation networks [39, 72].

The cytoskeleton represents yet another type of biological network. It is composed of actin filaments (AFs), microtubules (MTs), and intermediate filaments that form intricate interconnected arrays. Plant cells lack intermediate filaments, and their actin and microtubule cytoskeleton exhibits structural and functional differences to that of animal and yeast cells. These differences may be due to the presence of a rigid cell wall, a large central vacuole, the absence of discrete cytoskeleton organizing centers, or the general need of plants, as sessile organisms, to cope with changing environmental conditions [17, 68].

In plant interphase cells, AFs exhibit extraordinarily dynamic behaviors [60]. A major function of the actin cytoskeleton is to support cytoplasmic streaming, the directed flow of cytosol and organelles, which is mainly powered by ATP-driven myosin movement of compartments along the actin cytoskeleton [59, 63]. Further-

more, recent studies have shown that transportation of organelles depends on the micro-environment of the actin structures, where organelles are rapidly transported along actin bundles and display reduced motility when surrounded by thin AFs [1, 54].

The behavior of single MTs, as well as MT arrays, has been described throughout the cell cycle and for different cell types [10, 35, 69]. Their dynamics has been well-characterized [16, 17, 33], and can lead to the formation of self-organized patterns that largely explain the MTs' orientation in growing cells [2, 44, 64, 77]. While MTs sustain vesicle motility in certain plant cells [12], they are typically located at the cell cortex and support the synthesis of cellulose microfibrils in interphase cells [51]. Nevertheless, there is emerging evidence for transport along MTs also in these cell types, e.g., Golgi and small cellulose containing compartments have been reported to track along cortical MTs [14].

Several studies have investigated the mechanical properties of the cytoskeleton in yeast and animal cells both experimentally [43, 66] and theoretically [7, 46, 66]. Models of AFs as a system of stiff, spring-connected rods have demonstrated a percolation-related transition in the viscoelastic properties [21, 76], similar to signal propagation in a cytoskeleton model of connected rods [57, 58].

The above studies employed a bottom-up approach in which the behavior of a system is explained based on the dynamics of its components. However, the interconnected structure and the rapid dynamics of the cytoskele-

ton lend themselves to a top-down approach, which is independent of detailed molecular knowledge and better suited for uncovering the principles underlying cytoskeletal organization. Two studies have used such an approach in animal systems: AF arrays have been described as a superposition of different tessellation models [20] and a theoretical investigation of cytoskeletal transport in a system with passive diffusion and active transport along a random network of segments has demonstrated different regimes of transport [47]. Therefore, there is need for a network-based representation of the cytoskeleton that: (1) captures its complex network structure, (2) is based on biologically solid ground, (3) can be used to describe dynamic network processes, and (4) may uncover organizational principles of the cytoskeleton in plant and animal cells.

In this study, we propose a novel framework that captures the structure and dynamics of the actin and microtubule cytoskeleton as complex networks. We used this framework to quantify and compare the behavior of AFs and MTs in plant interphase cells under different conditions. We tested the hypothesis that the cytoskeleton is well-suited to support transport processes. By developing suitable null models as references, we show that the cytoskeleton indeed exhibits biologically desirable transport-related properties, such as short average path lengths and high robustness against disruptions of the network. Finally, we demonstrate that man-made transportation networks display similar properties. The developed framework is readily applicable to study the cytoskeleton of other organisms or under different conditions.

## II. RESULTS

### A. Reconstruction of complex networks from cytoskeletal images

To investigate the networks of AFs and MTs, we grew *Arabidopsis* (*A. thaliana*) FABD:GFP and TUA5:mCherry dual-labeled seedlings [55] in the dark and imaged elongating hypocotyl cells. To capture rapid changes and to minimize bleaching, we used a spinning-disk confocal microscope (Fig. 1A and B; see electronic supplemental material (ESM) S1). To generate complex networks from the cytoskeleton image series we followed a two-step procedure: We placed a grid over the cytoskeleton which covers the cell’s cytoskeleton (e.g. Fig. 1C). From the grid, we constructed an edge-weighted network in which nodes represent the grid’s junctions, and edges represent the grid’s links. We assigned a weight to each edge by creating convolution kernels with Gaussian profiles for each edge (Fig. 1D), thus projecting the cytoskeleton onto the overlaid grid. This results in a weighted, undirected network (Fig. 1E) where the weights reflect the intensity of the underlying filaments/bundles. Using confocal z-stack image series,

these steps were also used to construct three-dimensional cytoskeletal networks (Fig. 1G). The procedure was repeated for all images of the recorded actin and microtubule time series, separately. As a result, each network captures information of the time-dependent cytoskeletal component whose properties may be readily investigated.

To determine if the studied network properties carry a biological signal, we developed several null models that randomize parts of the cytoskeletal structures while preserving the total amount of cytoskeleton in the cell (cf. Appendix A2). If a given network property is significantly higher or lower than expected by chance we conclude that the underlying cytoskeletal organization is non-random and, therefore, biological relevant. This may suggest that the cytoskeleton is tuned to guarantee such values of the structural or functional network property.

### B. The reconstructed networks capture biologically relevant features of the actin and microtubule cytoskeletal components

To test whether the proposed network-based approach captures biologically meaningful features, we used chemical treatments and environmental stimuli to alter the behavior of the cytoskeleton. First, we quantified the effect of the actin-disrupting drug Latrunculin B on the actin cytoskeleton. This drug binds to monomeric actin and, thereby, inhibits AF formation [75]. We reconstructed the AF networks for both the control and the treated plants for each frame of the image series. The structure of the AFs and their drug-induced fragmentation was quantified by two network properties which can be related to the biological phenomenon (see Appendix A3 for a mathematical description and detailed interpretation of these quantities): The standard deviation of the degree distribution [70] captures the spatial heterogeneity of the distribution of actin structures, i.e., images with regions of low and high cytoskeletal intensities yield both small and large edge weights and consequently a broader degree distribution (cf. Fig. 1E). Since the edge weights integrate intensities of possibly multiple filaments, our approach does not resolve differences in thicknesses or numbers of individual filament but only a combination thereof. By comparing the standard deviations of the degree distributions of control and treated plants, we found a statistically significant reduction by Latrunculin B (Fig. 2A; independent two-sample *t*-test:  $p$ -value =  $7.0 \cdot 10^{-9}$ ; for treated and non-treated plants, respectively, we pooled the standard deviations of the degree distributions across the first 20 time points of the image series). We then determined the average number of nodes per connected, non-trivial network component after thresholding the edge weights, providing an estimate for the extent to which the cytoskeletal filaments form connected networks. By using the 50th percentile as a threshold, we found that Latrunculin B reduces the average size of the resulting connected components (Fig. 2B;

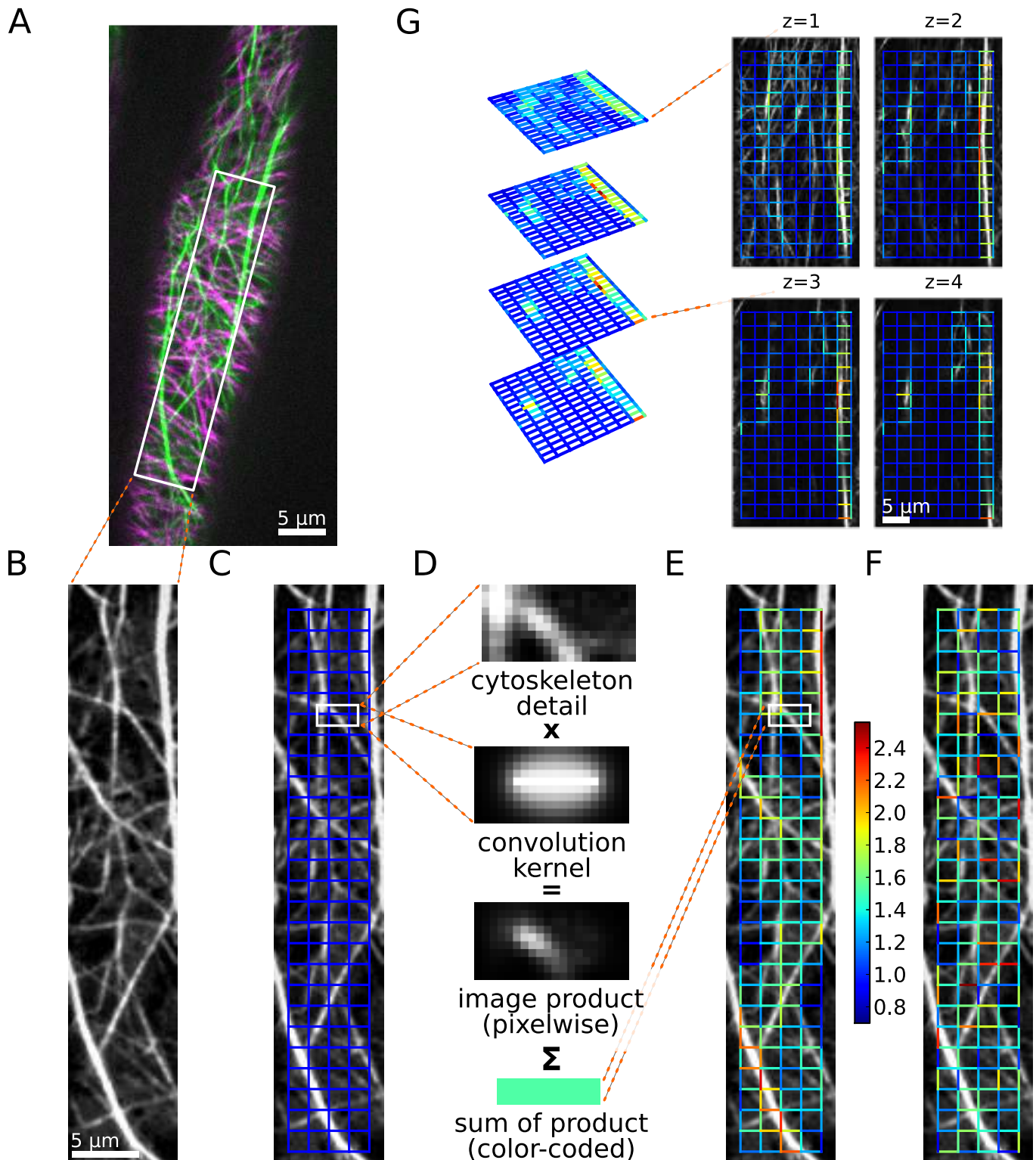
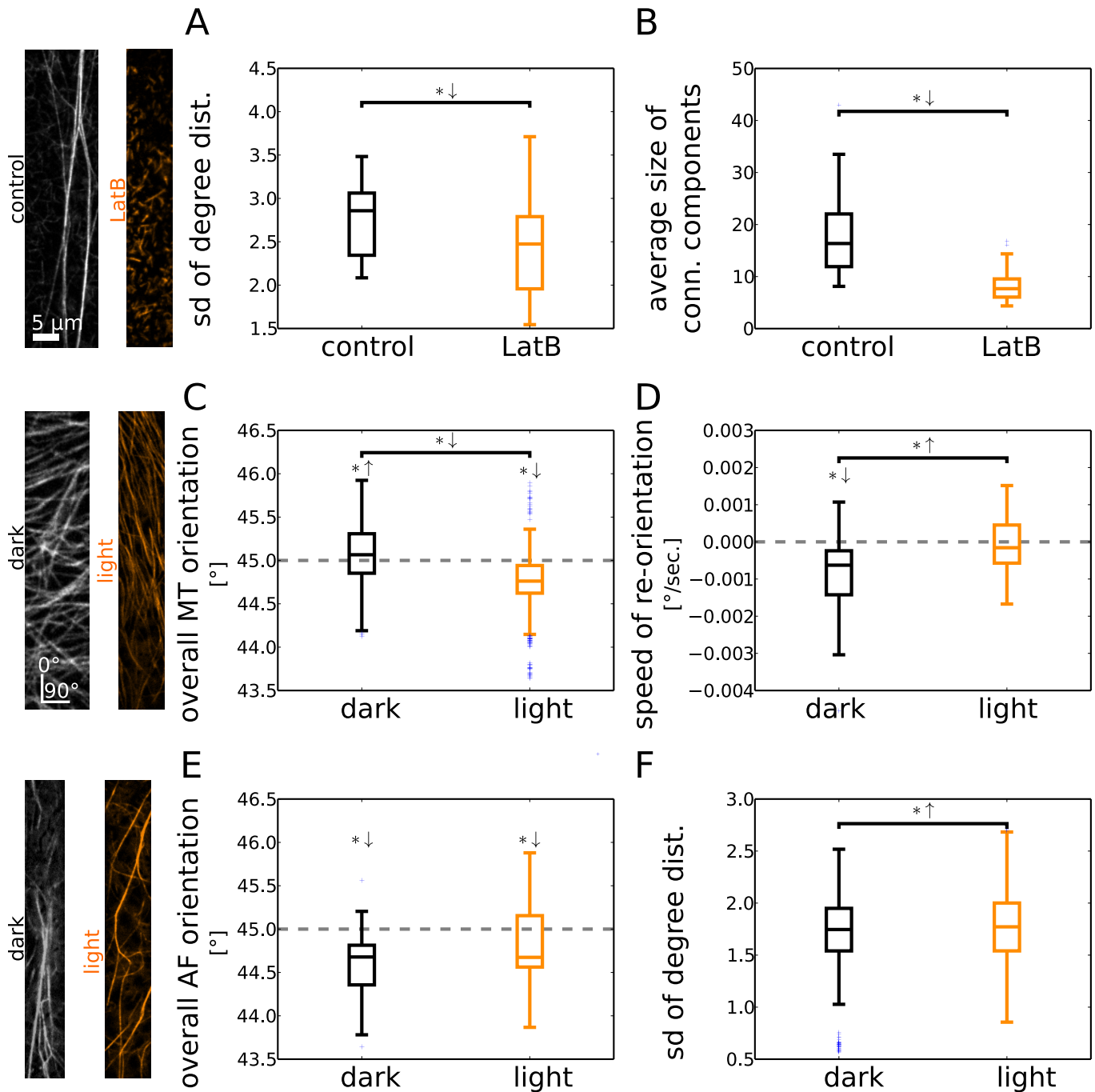


Figure 1. **From fluorescence image to reconstructed network, null model, and 3D extension.** (A) Colored overlay of unprocessed snapshots of the AFs (green) and MTs (magenta) of a dual-labeled, three-day-old *A. thaliana* hypocotyl cell. (B) Single preprocessed image of one cytoskeletal component, here AFs. (C) Grid used for network reconstruction (a uniform rectangular grid with 10 pixels spacings is shown in blue). (D) Using convolution kernels, the links of the grid are assigned scalar values by pixelwise multiplication of the kernel with the cytoskeleton image and subsequent summation. (E) Weighted, undirected network with edges given by the links of the chosen grid type and weights obtained via the kernel method (weights are color-coded from blue to red). (F) To assess the biological relevance of various properties of the cytoskeletal network, a null model is introduced through an ensemble of networks with shuffled edge weights (one exemplary realization is depicted). (G) From confocal z-stack recordings, a three-dimensional cytoskeletal network is reconstructed (grid spacings are 20 pixels; edges connecting different z-layers are set transparent for better visibility of the full network).



**Figure 2. Network properties capture biologically relevant aspects of cytoskeletal organization for different scenarios.** The first 20 frames of the image series are used for the analysis. \*  $\downarrow$  and \*  $\uparrow$  above a bar denote a decrease or increase of the properties of the treated relative to those of the control plants (independent two-sample  $t$ -test:  $p$ -value  $< 0.05$ ). \*  $\downarrow$  and \*  $\uparrow$  above a box plot denote network properties that fall below or exceed a reference value marked by a gray, dotted line (one-sample two-sided  $t$ -test:  $p$ -value  $< 0.05$ ). **(A)** The AF network of Latrunculin B-treated plants displays a smaller standard deviation of the network's degree distribution. **(B)** The connected patches of AFs are smaller after Latrunculin B treatment. **(C)** The orientation of MTs is predominantly horizontal in dark-grown plants and vertical in light-exposed plants. **(D)** Computing the change in MT orientation per unit time shows a difference between control and light-treated plants. In dark-grown plants, a significant change towards a vertical orientation is observed, which is absent for light-treated plants. **(E)** The (horizontal) orientation of AFs is not altered in plants exposed to light. **(F)** Light induces a dispersion of AFs which yields a broader degree distribution.



independent two-sample  $t$ -test:  $p$ -value =  $2.9 \cdot 10^{-42}$ ). These findings are in agreement with visual reports on the fragmented actin structure of Latrunculin B-treated cytoskeletons [75].

By using the reconstructed MT network, we quantified the overall orientation of MTs in plants that had been exposed to light several hours before imaging. Light is one of the environmental factors that determine plant growth, and it is well established that the MT array rapidly changes from largely transverse to a generally longitudinal when seedlings are exposed to light [50, 53, 74]. As our method does not detect individual filaments, we inferred the MT orientation indirectly (see Appendix A4 for a detailed derivation): By placing an imaginary rod of a specific length and orientation over the grid we calculated its contributions to the weights of edges with different orientations by using our kernel method (cf. Fig. 1D). Here, we solved the inverse problem to obtain the overall MT orientation  $\alpha$  from the weight distribution of edges with different orientations. Angles  $\alpha \in [0^\circ, 45^\circ)$  and  $\alpha \in (45^\circ, 90^\circ]$  indicate overall vertical and horizontal orientations of the MTs, respectively. We estimated the MT orientation for seedlings grown under dark and light conditions and found a significant difference (Fig. 2C; independent two-sample  $t$ -test:  $p$ -value =  $5.8 \cdot 10^{-52}$ ) with a horizontal and longitudinal orientation, respectively (one-sample two-sided  $t$ -tests: dark  $p$ -value =  $6.3 \cdot 10^{-8}$ , light  $p$ -value =  $4.7 \cdot 10^{-45}$ ). These findings are in agreement with known results [25, 50, 53, 55]. They further revealed that despite the strong correlation between light exposure and longitudinal MT orientation, there are also deviants (cf. Fig. 2C): Under dark condition, a fraction of about 40% of the MT networks shows an, unexpected, overall vertical orientation while under light conditions, about 20% of the analyzed MT networks display an overall horizontal orientation, contrary to expectations. These deviations from the expected results may highlight the inherent variability of cytoskeletal responses to external stimuli and support the view that hypocotyl cells may be in different stages of growth [23, 41, 53].

We also studied the speed of MT reorientation under the microscope by computing the slope of the average orientation time series via a linear regression. There was a significant difference between the two treatments (Fig. 2D; independent two-sample  $t$ -test:  $p$ -value =  $2.5 \cdot 10^{-3}$ ), i.e., while the change in orientation is negative in dark, it does not significantly differ from zero in light (one-sample two-sided  $t$ -test: dark  $p$ -value =  $2.5 \cdot 10^{-5}$ , light  $p$ -value = 0.6). Therefore, we conclude that over the range of five minutes of the experiment the confocal laser light does induce a reorientation of the MTs towards the longitudinal cell axis in dark-grown plants; however, this is not the case in plants exposed to light before imaging as reorientation of MTs has already progressed further in these cells.

Next, we employed our network-based framework to investigate the behavior of AFs in response to light in growing hypocotyls. Like for MTs, we inferred the overall

orientation of the AFs for dark-grown and light-treated plants, respectively. We found no significant difference in actin orientation between the treatments (Fig. 2E; independent two-sample  $t$ -test:  $p$ -value =  $6.6 \cdot 10^{-2}$ ), with a consistent major longitudinal orientation (one-sample two-sided  $t$ -test: dark  $p$ -value =  $3.8 \cdot 10^{-7}$ , light  $p$ -value =  $4.4 \cdot 10^{-2}$ ). To quantify the heterogeneity of the actin distribution, we computed the standard deviation of the degree distributions for both scenarios. In light-treated plants, the actin cytoskeleton displayed a more heterogeneous distribution across the cell than in dark-grown plants (Fig. 2F; independent two-sample  $t$ -test:  $p$ -value =  $1.5 \cdot 10^{-4}$ ), implying the prevalence of bundles. These findings agree with reports on the impact of light on the organization of AFs in maize coleoptiles [67]. However, they do not agree with the qualitative findings in a different species, i.e., rice, where light was shown to promote a change in AF orientation from transverse to longitudinal and to disperse actin bundles [31]. Interestingly, the rearrangement of AFs under light has been linked to that of MTs [55]. Therefore, our findings suggest that a change in environmental conditions would impose a need for rapid redistribution of cellular material in the cell, which are known to be facilitated by actin bundles [1].

### C. Accessibility and robustness of cytoskeletal networks

After demonstrating the inherent ability of our network approach to capture biologically relevant information on cytoskeletal organization, we focused on identifying network properties that reflect the functions of the cytoskeleton. To investigate the transport efficiency of the AF and MT networks (Fig. 3A), we computed average path length (as a measure for the cellular accessibility of the cytoskeleton) and algebraic connectivity (as a measure for the cytoskeletons' robustness against disruptions) (see Appendix A3 for the mathematical formulation and a detailed interpretation of the properties).

The average (shortest) path length (APL) [70] is the average of the minimum distances between all pairs of nodes in a (edge-weighted) network. Here, the length of an edge is given by the inverse of its weight, i.e., thick actin bundles or tubulin filaments yield small edge lengths. This is reasonable since cytoskeletal bundles typically facilitate faster transport compared to thinner filaments [1] which may, in general, depend on the size of the cargo. The APL provides an estimate of how close any two nodes are expected to be and, hence, the accessibility in the cytoskeleton. By computing the APLs for the sequence of the AF and MT networks, we obtained two time series (Fig. 3B, green and magenta, solid lines). The corresponding values largely reflect the overall intensity distribution of the images and, by themselves, carry little information about the underlying network structure. As a reference, we calculated the APLs

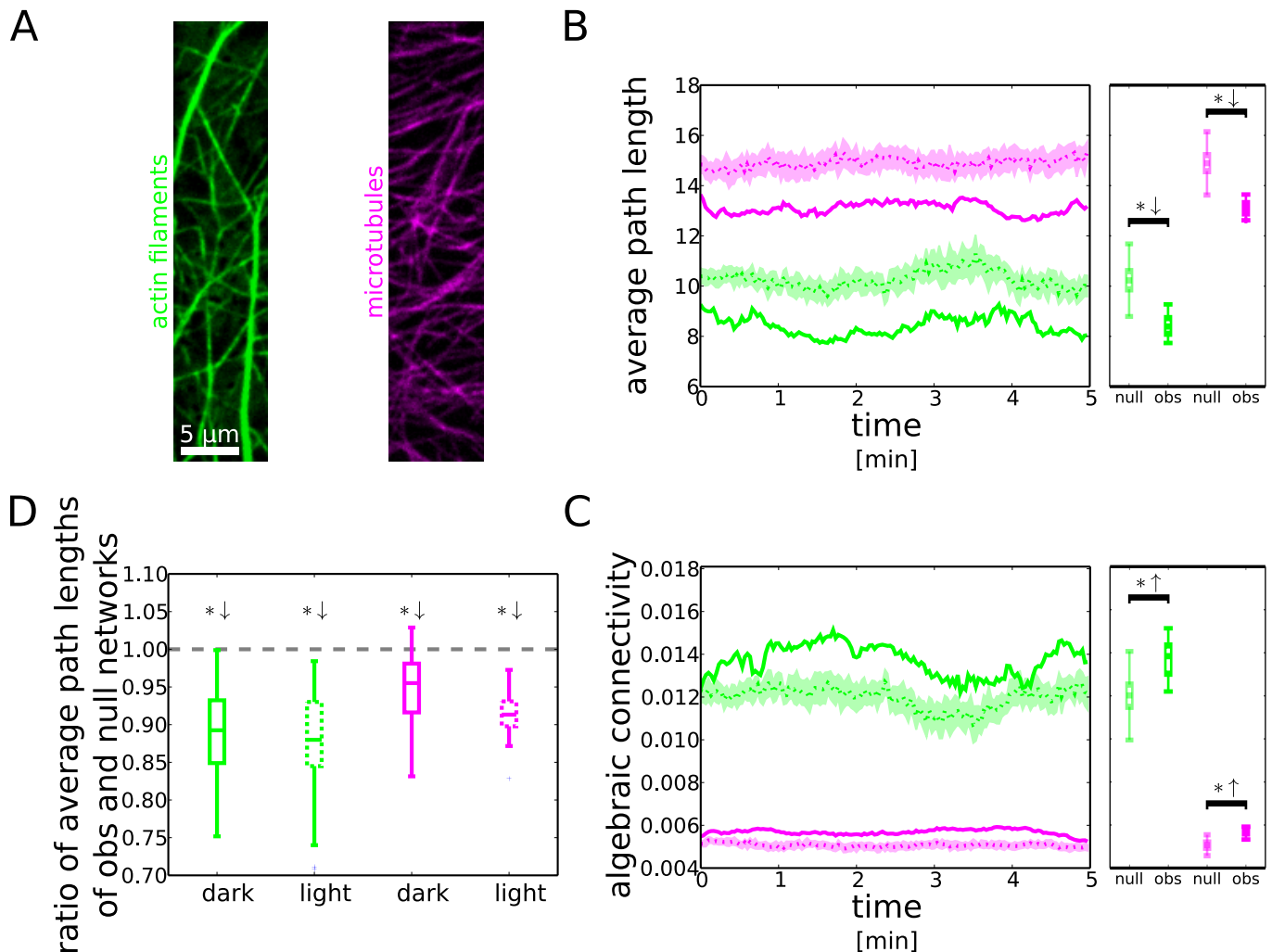


Figure 3. **Time-resolved average path length and algebraic connectivity of cytoskeletal networks and null model networks.** In (B) and (C), the results for the observed networks (solid lines) of AFs (green) and MTs (magenta) are compared to those of the null model (dashed lines: ensemble-mean; shaded regions: ensemble-mean  $\pm$  standard deviation). The box plots show the distribution of values of a network property used in the statistical test. (A) Green- and magenta-colored images of AFs and MTs, respectively. (B) The average path lengths of AF and MT networks (solid lines) fluctuate over time and stay well below the average path lengths of the null model (dashed lines and shaded regions). (C) The algebraic connectivity is consistently larger for both AFs and MTs in the observed cytoskeletal networks (solid lines) than in the null model networks (dashed lines and shaded regions). (D) Comparing the ratios of average path lengths of the observed networks and their null model networks for AFs and MTs yields no statistically significant difference between dark and light conditions.

for ensembles of AF or MT null model networks, i.e., networks obtained by shuffling edge weights (Fig. 3B, green and magenta, dashed lines and shaded regions). We found that the observed networks exhibit significantly smaller APLs than their respective null models (independent two-sample  $t$ -test: AF  $p$ -value =  $7.8 \cdot 10^{-273}$ , MT  $p$ -value <  $2.2 \cdot 10^{-308}$ ).

The algebraic connectivity (AC) [70] is the second smallest eigenvalue of the network's graph Laplacian, which is closely related to the weight matrix of the network, and reflects how well-knit the network is. While a vanishing AC indicates the decomposition of the network into two or more disconnected components, larger values correspond to a higher robustness of the network

against disruptions. By comparing the AC of the observed actin and microtubule networks (Fig. 3C, green and magenta, solid lines) to their null model counterparts (Fig. 3C, green and red, dashed lines and shaded regions), we found that the observed networks yield significantly larger algebraic connectivities than their respective null model networks (independent two-sample  $t$ -test: AF  $p$ -value =  $7.5 \cdot 10^{-139}$ , MT  $p$ -value =  $2.9 \cdot 10^{-278}$ ).

These findings may be graphically explained as follows: Networks of MTs, and even more so AFs, possess filaments and bundles that stretch across large parts of the cell. These structures establish connected paths in the networks with large weights and therefore small lengths. In the computation of shortest path lengths, they act as

“highways” that efficiently connect spatially distant regions. Furthermore, the AF and MT networks exhibit larger regions that are particularly strongly linked and result in a higher robustness of the networks against disruption. To support this interpretation, we computed the degree assortativity [48] given by the correlation between degrees of nodes and those of their neighbors. It quantifies the extent to which nodes of (dis-)similar degree are connected to each other. Both the AF and MT networks exhibit significantly higher assortativity than their corresponding null model networks and are hence more spatially clustered (independent two-sample  $t$ -tests: AF  $p$ -value  $< 2.2 \cdot 10^{-308}$ , MT  $p$ -value  $< 2.2 \cdot 10^{-308}$ ). We note that both APL and AC are summary statistics that do not capture differences in local connectivity patterns but reflect network properties that relate to the network’s overall transport capacity.

Interestingly, despite the differences in the network architecture of AFs and MTs under dark and light conditions (cf. Fig. 2), there were no significant differences in the ratios of APLs of observed and null model networks (Fig. 3D). Moreover, these ratios stay consistently below one throughout the time series (one-sample two-sided  $t$ -tests:  $p$ -values  $< 0.05$  for AF/MT dark/light), reflecting small effort for reaching any part of the cytoskeletal networks. Thus, the cytoskeleton preserves its advantageous transport properties over time and across conditions.

While the MT network can largely be captured at the cell cortex in interphase cells, the actin cytoskeleton constitutes a three-dimensional structure that spans the expanding cell. To ensure that we captured the volumetric behavior of the AFs, we also recorded confocal z-stack image series of such cells and used our framework to reconstruct the AF network as a three-dimensional network (cf. Fig. 1G). To assess if the additional information about AFs below the cortical plane changes the transport efficiency of the AF network, we compared the APL and AC of the three-dimensional network to that of the two-dimensional network obtained by averaging the intensities of edges at the same x-y-position across all z-layers. In both cases, the ratio of network properties of the observed network and the null model networks stays well below one (one-sample two-sided  $t$ -test:  $p$ -values  $< 0.05$  for 2D/3D APL/AC; see Appendix A2 for details). Analogously to the bundle structures in the 2D networks, the actin structures that reach deeper into the cell provide strong connections in the 3D reconstruction (see Fig. 1G) that naturally equip the network with shorter paths and higher robustness.

Taken together, AF as well as MT networks display highly non-random features. In particular, short APL (good accessibility) and large AC (high robustness) are preserved over time and across different environmental conditions. These findings provide quantitative support for the idea that plants reliably establish and maintain cytoskeletal structures that are optimized for transport processes throughout the cell [51, 54, 59].

## D. The cytoskeleton and the German autobahn exhibit similar network properties

We next asked whether the observed efficiency in network properties is unique to the cytoskeleton or if it can also be observed in other transportation networks. As a prominent example, we generated images of the German autobahn with color-coded speed limits (Fig. 4A; The maximum speed limit is set to 200 km/h, the speed limit outside of the autobahn is set to 50 km/h. However, our findings are largely independent of this choice, see Appendix A5). By using our established framework, we obtained a weighted network for the autobahn (Fig. 4B) and corresponding null model networks by shuffling edge weights. For the APL and the AC, we computed the ratios for the respective network properties of the autobahn and its null model networks and we found that the autobahn network exhibits shorter APLs and higher algebraic connectivities than expected by chance (Fig. 4I, black). These results are similar to what we found for the cytoskeleton (Fig. 4I, green and magenta). Furthermore, we note that the degree distributions of the cytoskeletal networks and the autobahn are unimodal and peak around their means (Fig. 4E and F).

To differentiate these networks from networks with different structural and transport-related properties, we further studied a contrived network with a stronger local structure and weaker long-ranged connections (Fig. 4C). The contrived network displays a heavy-tailed degree distribution (Fig. 4G) as well as properties associated with poor transport efficiency, namely, longer APL and smaller AC than expected from the null model (Fig. 4I, orange).

Another interesting comparison is that of the cytoskeleton and the autobahn to networks in which one or several transport-related properties are optimized. The weight distribution of a network with a fixed sum of edge weights and maximal AC may be computed efficiently by solving a semi-definite optimization problem whose solution is unique [9, 62] (Fig. 4D). Such an optimally robust network outperforms the cytoskeletal and the autobahn networks by a factor of eight with respect to the ratio of AC of observed and null model networks (Fig. 4I, blue). However, it is less efficient in terms of its APL, which is higher than expected by chance, demonstrating a trade-off between different measures of network optimality.

While there are certainly differences in the structure as well as the function of the cytoskeleton and the autobahn, the network properties studied here are summary statistics and it is not possible to infer local structural differences from them. In particular, we do not study their absolute values but the relative efficiency of these networks with respect to their respective null model which may point to its organizational principles.

To conclude, both the actin and microtubule cytoskeleton display characteristics typical of transportation networks, such as the autobahn, and exhibit structures which may not be aimed at optimizing a single prop-

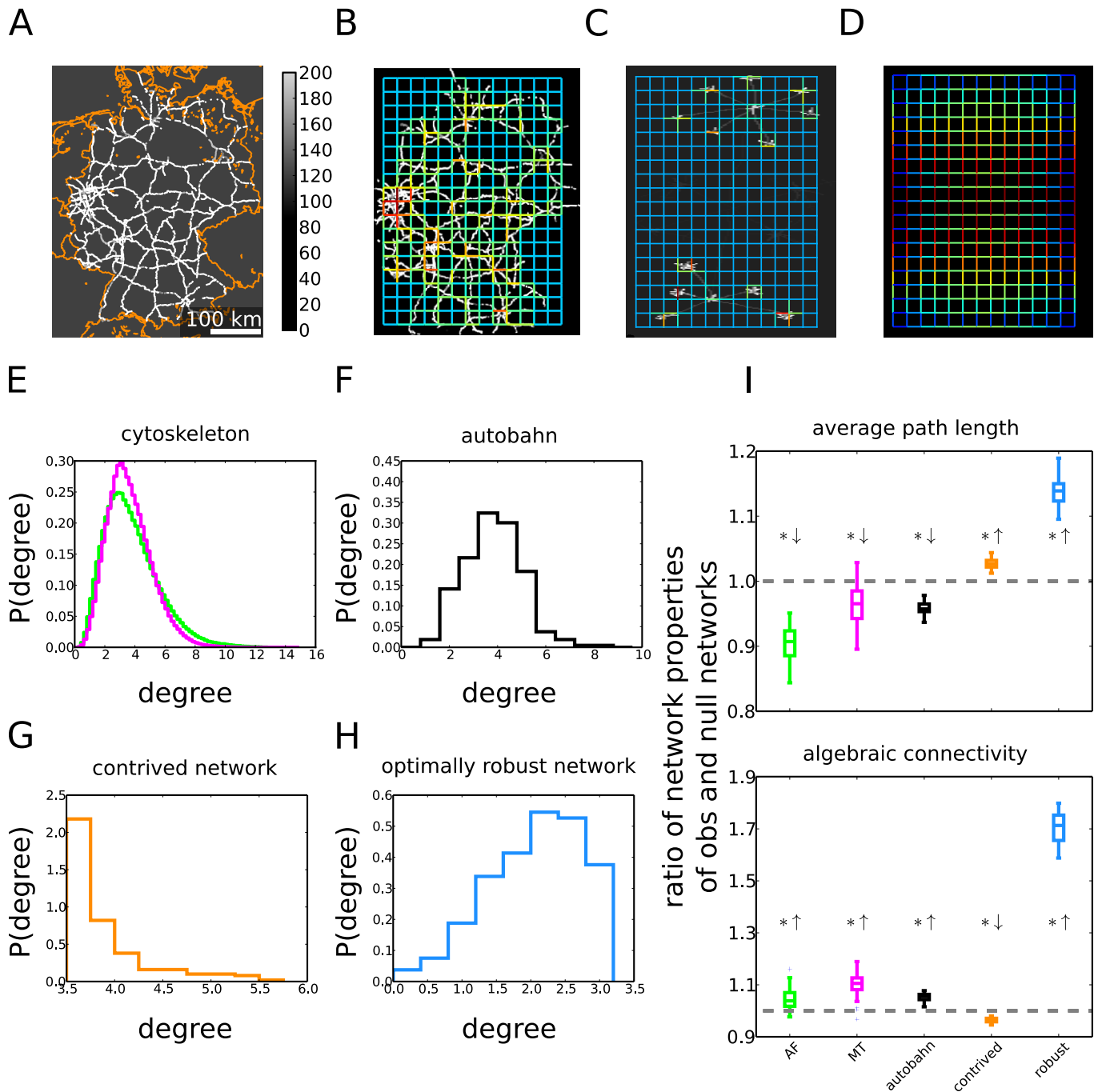


Figure 4. **Comparison of cytoskeleton, German autobahn, and other types of networks.** (A) The autobahn network of Germany with color-coded speed limits and national borders (orange) for guidance. (B) Network reconstructed from the autobahn image. (C) Reconstructed network for a contrived underlying structure with different structural and transport-related properties. (D) Network with maximal algebraic connectivity for the given grid-topology and normalized sum of weights (here, the network is constructed via an optimization procedure and not inferred from an underlying image intensity distribution; the black background is for better visibility only). (E) The degree distributions of the AF (green) and MT (magenta) networks are unimodal and peak around their means (excess kurtosis  $> 0$ ; the resolution of the histograms is higher as they include all networks of an image series, cf. Fig. 3). (F) The degree distribution of the autobahn network is unimodal and peaks around its mean (excess kurtosis  $> 0$ ). (G) For the contrived network, the degree distribution is also peaked (excess kurtosis  $> 0$ ) but shows a more heavy right tail compared to (E) and (F). (H) The degree distribution of the optimally robust network is broader around the peak and has thinner tails (kurtosis  $< 0$ ). (I) The ratios of average path lengths of observed and null model networks are below one for the cytoskeletal and the autobahn networks and above one for the contrived and the optimally robust network. The algebraic connectivities are bigger than expected by chance for all studied networks, except for the contrived networks that show a smaller algebraic connectivity. All deviations from the unit ratio are statistically significant (one-sample two-sided  $t$ -tests: all  $p$ -values  $< 0.05$ ).

erty indicative of efficient transport. Our data therefore provide quantitative measures to support a view of the plant interphase cytoskeleton as an efficient transportation network.

### III. DISCUSSION

Though many studies have analyzed the cytoskeleton, most of them have relied on qualitative observations or manual tracking of up to some dozens of AFs and MTs. The rapid dynamics, as well as strong variability of cytoskeletal organization across different cell types, stages of cell life, and environmental conditions, necessitate a framework that allows for a fast and objective quantification of the cytoskeletal components in living cells. This would then allow for biologically meaningful interpretations that go beyond strictly theoretical studies to investigate the structure of the system. Here, we described one such framework that captures biologically relevant variations.

Many studies have used a bottom-up approach to the cytoskeleton, in which the molecular principles are presupposed and used to infer the behavior of the system. Instead, we pursued a top-down strategy to represent the cytoskeletal organization without the need for detailed molecular knowledge. Hence, our approach hints at the underlying organizational principles of the cytoskeleton. More specifically, by choosing a representation through complex networks, we could exploit the well-equipped toolkit from graph theory to investigate the structure of the cytoskeleton and its relation to, e.g., efficient transport processes in the cell.

For a careful interpretation of these findings, we need to bear in mind several points: (1) Our network reconstruction method creates nodes at positions given by the chosen grid (cf. Fig. 1). Hence, not all nodes correspond to crossings of the filaments. Moreover, despite our focus on the largely planar cortical cytoskeletal even apparently crossing filament maybe separated by hundreds of nanometers in z-direction. Using our current imaging techniques, such distances may not be resolved in the 3D reconstruction either (see outlook below). In particular, such distances prohibit the switching of motor proteins (cf. e.g. [4] for MT). Yet, the edge weights in our method agglomerate local intensities that may originate from multiple filaments in different depths. More importantly, typical cargo such as mitochondria, Golgi bodies, or chloroplasts range from several 100 nm to several  $\mu\text{m}$  in size and may thus easily bridge even larger distances between filaments, thereby justifying our assumption of transport along edges and via nodes. (2) In our approach, all edges are undirected, i.e., they allow bi-directional transport. While bi-directional transport may occur along single actin or microtubular filaments, e.g., due to different motor proteins or fluctuations [11, 26, 42], bundles of filaments typically allow uni-directional only. This uni-directionality is further

amplified by the cytoplasmic bulk flow generated by the coordinated movement of motor proteins [59]. Yet again, our reconstruction methods assigns edge weights by integrating local intensities of possibly multiple filaments with different orientations. Thus, fully bi-directional of transport is unlikely (but not excluded) and, since it can not be inferred from the cytoskeletal images alone, we use it as an approximation of the potential transport capacity. (3) This potential transport capacity is modeled to be higher in regions with many/thick cytoskeletal filaments, as described by the edge weights. However, the edge weights do not quantify the speed/amount of cargo that is really transported (and we do not measure it, see outlook below). (4) Finally, we note that AF and MT networks generally transport different cargo (cf. [51, 59]), although there is evidence for transport of, e.g., small cellulose containing vesicle along both structures [24, 28]. In addition, different types of cells may require different modes of transportation [34]. Here, we focused on the potential transport capacity of the cytoskeleton in interphase hypocotyl cells, but our framework may readily be used to study other scenarios.

There is a rich literature on the comparison of structures of different networks. Many biological and man-made networks show scale-free degree distributions, i.e., there are a few nodes with many neighbors [8], e.g., airway networks [27]. However, nodes in other transportation networks are restricted regarding the number of potential neighbors due to the physical limitations. Road and railway networks display degree distributions that peak around their average values [5], which we also demonstrated for the cytoskeletal networks. Despite the apparently diverse principles underlying man-made transportation networks, studies have revealed strong agreement in a number of their properties, e.g., degree distribution. This agreement may be explained by costs associated with the establishment of new nodes and links [6, 13, 45]. Our findings suggest that comparable cost-related restrictions may play a role in the formation of the cytoskeleton, leading to similar structures and transport properties as in man-made networks.

In summary, our framework captures the complex network structure of filamentous cytoskeletal components. We used this framework to derive organizational principles of the cytoskeleton. We further showed that AF and MT networks display biologically desirable characteristics, such as short APLs and high robustness, similar to characteristics found in non-biological transportation networks. In particular, these features of efficient transportation networks are maintained over time and across conditions.

Possible directions of future efforts are manifold: (1) Our framework can be employed to quantify the complex structures of AF and MT networks, and thus enables an automated and objective comparison of the complex structures of cytoskeletal networks in other biological systems, e.g., focusing on the cytoskeleton connecting the nucleus to other parts of the cell. (2) The resolution

of the fine cytoskeletal structures may be improved by using more advanced imaging techniques like total internal reflection fluorescence microscopy, at least for the cortical cytoskeleton. (3) Another promising direction is the comparison of reconstructed cytoskeletal networks to networks that optimize one or several seminal network properties. As different network structures favor specific properties, the cytoskeleton may represent an evolutionarily shaped compromise between them. While such a balance has been suggested, e.g., between the speed and the sensitivity in the polarization of the cytoskeleton [30], quantitative evidence for a trade-off in the cytoskeleton's transport properties is lacking. We note that besides its vital role in cellular transport processes the plant cytoskeleton strikingly determines the mechanical properties of the cell. (4) Finally, our work paves the way for direct studies of the cytoskeleton as a transportation network. Employing actin and organelle dual-labeled plants, it is appealing to correlate actual biological transport processes with flow-related network measures. While several studies have investigated the transport of organelles and vesicles along the cytoskeleton [4, 24, 52, 59], none have quantitatively linked it to the complex structure of the cytoskeletal network. Answering these questions may contribute to a better understanding of the organizing and dynamic principles of the cytoskeleton.

#### IV. MATERIALS AND METHODS

The experiment setup includes dual-labeled *Arabidopsis thaliana* Columbia-0 seedlings to which different treatments were applied prior to imaging in a spinning

disk confocal microscope setup. For further details, refer to Appendix A1. The computational network-based investigation of the image series, as illustrated in Fig. 1, includes: (1) the preprocessing of the images in Fiji [56], (2) the creation and quantification of the weighted cytoskeletal and null model networks, and (3) their statistical analyses in Python [65] (using SciPy [37], NumPy [49], NetworkX [29] and the Matplotlib [32] libraries). The construction of an optimally robust network was performed by solving a semi-definite optimization problem using the Cvxopt Python package [15]. Detailed descriptions of these steps are given in Appendix A2 and the studied network properties are described in detail in Appendix A3. The overall orientation of cytoskeletal components is inferred from the network's weight distribution as described in Appendix A4. The data of the German autobahn, as depicted in Fig. 4, are collected from OpenStreetMap and filtered as explained in Appendix A5.

#### V. ACKNOWLEDGMENTS

D.B., A.I., S.P., and Z.N. were supported by the Max-Planck-Gesellschaft. We thank Dr. Tijs Ketelaar and Dr. Georg Basler for valuable comments on the manuscript.

#### VI. ABBREVIATIONS LIST

AF: actin filament, MT: microtubule, APL: average path length, AC: algebraic connectivity

- 
- [1] Akkerman, M., Overdijk, E. J., Schel, J. H., Emons, A. M. C., and Ketelaar, T. (2011). Golgi body motility in the plant cell cortex correlates with actin cytoskeleton organization. *Plant Cell Physiol*, 52(10):1844–1855.
  - [2] Allard, J. F., Ambrose, J. C., Wasteneys, G. O., and Cytrynbaum, E. N. (2010). A mechanochemical model explains interactions between cortical microtubules in plants. *Biophys J*, 99(4):1082–1090.
  - [3] Arganda-Carreras, I., Sorzano, C. O., Marabini, R., Carazo, J. M., Ortiz-de Solorzano, C., and Kybic, J. (2006). Consistent and elastic registration of histological sections using vector-spline regularization. In Beichel, R. R. and Sonka, M., editors, *Computer vision approaches to medical image analysis*, pages 85–95. Springer Berlin Heidelberg.
  - [4] Bálint, S., Verdeny Vilanova, I., Sandoval Álvarez, A., and Lakadamyali, M. (2013). Correlative live-cell and superresolution microscopy reveals cargo transport dynamics at microtubule intersections. *Proc Natl Acad Sci*, 110(9):3375–3380.
  - [5] Barthélemy, M. (2011). Spatial networks. *Phys Rep*, 499(1):1–101.
  - [6] Barthélemy, M. and Flammini, A. (2008). Modeling urban street patterns. *Phys Rev Lett*, 100(13):138702.
  - [7] Benetatos, P. and Zippelius, A. (2007). Anisotropic random networks of semiflexible polymers. *Phys Rev Lett*, 99(19):198301.
  - [8] Bornholdt, S. and Schuster, H. G. (2003). *Handbook of graphs and networks*, volume 2. Wiley Online Library, Hoboken, New Jersey, USA.
  - [9] Boyd, S. (2006). Convex optimization of graph laplacian eigenvalues. In Marta Sanz-Solé, Javier Soria, J. L. V. J. V., editor, *Proceedings of the International Congress of Mathematicians*, volume 3, pages 1311–1319. European Mathematical Society Publishing House.
  - [10] Buschmann, H., Green, P., Sambade, A., Doonan, J., and Lloyd, C. (2011). Cytoskeletal dynamics in interphase, mitosis and cytokinesis analysed through agrobacterium-mediated transient transformation of tobacco by-2 cells. *New Phytol*, 190(1):258–267.
  - [11] Caviston, J. P. and Holzbaur, E. L. F. (2006). Microtubule motors at the intersection of trafficking and transport. *Trends Cell Biol*, 16(10):530–537.
  - [12] Collings, D. (2008). Crossed-wires: interactions and cross-talk between the microtubule and microfilament



- networks in plants. In *Plant microtubules*, pages 47–79. Springer Berlin Heidelberg.
- [13] Courtat, T., Douady, S., and Gloaguen, C. (2011). Centrality maps and the analysis of city street networks. In Samson Lasaulce, Dieter Fiems, P. H. L. V., editor, *Proc 5th Internat ICST Conf Perform Eval Method and Tools*, pages 316–321, Brussels, Belgium. ICST.
- [14] Crowell, E. F., Bischoff, V., Desprez, T., Rolland, A., Stierhof, Y.-D., Schumacher, K., Gonneau, M., Höfte, H., and Vernhettes, S. (2009). Pausing of Golgi bodies on microtubules regulates secretion of cellulose synthase complexes in Arabidopsis. *Plant Cell Online*, 21(4):1141–1154.
- [15] Dahl, J. and Vandenberghe, L. (2006). Cvxopt: a Python package for convex optimization.
- [16] Ehrhardt, D. W. (2008). Straighten up and fly right: microtubule dynamics and organization of non-centrosomal arrays in higher plants. *Curr Opin Cell Biol*, 20(1):107–116.
- [17] Ehrhardt, D. W. and Shaw, S. L. (2006). Microtubule dynamics and organization in the plant cortical array. *Annu Rev Plant Biol*, 57:859–875.
- [18] Fell, D. and Wagner, A. (2000). The small world of metabolism. *Nat Biotechnol*, 18(11):1121–1122.
- [19] Felleman, D. J. and Van Essen, D. C. (1991). Distributed hierarchical processing in the primate cerebral cortex. *Cereb Cortex*, 1(1):1–47.
- [20] Fleischer, F., Ananthakrishnan, R., Eckel, S., Schmidt, H., Käs, J., Svitkina, T., Schmidt, V., and Beil, M. (2007). Actin network architecture and elasticity in lamellipodia of melanoma cells. *New J Phys*, 9(11):420.
- [21] Forgacs, G. (1995). On the possible role of cytoskeletal filamentous networks in intracellular signaling: an approach based on percolation. *J Cell Sci*, 108(6):2131–2143.
- [22] Gazit, Y., Berk, D. A., Leunig, M., Baxter, L. T., and Jain, R. K. (1995). Scale-invariant behavior and vascular network formation in normal and tumor tissue. *Phys Rev Lett*, 75(12):2428–2431.
- [23] Gendreau, E., Traas, J., Desnos, T., Grandjean, O., Caboche, M., and Hofte, H. (1997). Cellular basis of hypocotyl growth in Arabidopsis thaliana. *Plant Physiol*, 114(1):295–305.
- [24] Goode, B. L., Drubin, D. G., and Barnes, G. (2000). Functional cooperation between the microtubule and actin cytoskeletons. *Curr Opin Cell Biol*, 12(1):63–71.
- [25] Granger, C. and Cyr, R. (2001). Spatiotemporal relationships between growth and microtubule orientation as revealed in living root cells of Arabidopsis thaliana transformed with green-fluorescent-protein gene construct GFP-MBD. *Protoplasma*, 216(3):201–214.
- [26] Gross, S. P. (2004). Hither and yon: a review of bi-directional microtubule-based transport. *Phys Biol*, 1(2):1–11.
- [27] Guimerà, R., Mossa, S., Turtschi, A., and Amaral, L. N. (2005). The worldwide air transportation network: anomalous centrality, community structure, and cities’ global roles. *Proc Natl Acad Sci*, 102(22):7794–7799.
- [28] Gutierrez, R., Lindeboom, J. J., Paredez, A. R., Emons, A. M. C., and Ehrhardt, D. W. (2009). Arabidopsis cortical microtubules position cellulose synthase delivery to the plasma membrane and interact with cellulose synthase trafficking compartments. *Nat Cell Biol*, 11(7):797–806.
- [29] Hagberg, A., Swart, P., and Chult, D. (2008). Exploring network structure, dynamics, and function using networkx. Technical report, Los Alamos National Laboratory (LANL).
- [30] Hawkins, R. J., Tindemans, S. H., and Mulder, B. M. (2010). Model for the orientational ordering of the plant microtubule cortical array. *Phys Rev E*, 82(1):011911.
- [31] Holweg, C., Süßlin, C., and Nick, P. (2004). Capturing in vivo dynamics of the actin cytoskeleton stimulated by auxin or light. *Plant Cell Physiol*, 45(7):855–863.
- [32] Hunter, J. D. (2007). Matplotlib: a 2D graphics environment. *Comput Sci and Engr*, 9(3):90–95.
- [33] Hush, J., Wadsworth, P., Callahan, D., and Hepler, P. (1994). Quantification of microtubule dynamics in living plant cells using fluorescence redistribution after photobleaching. *J Cell Sci*, 107(4):775–784.
- [34] Hussey, P. J., Ketelaar, T., and Deeks, M. J. (2006). Control of the actin cytoskeleton in plant cell growth. *Annu Rev Plant Biol*, 57:109–125.
- [35] Jacques, E., Lewandowski, M., Buytaert, J., Fierens, Y., Verbelen, J.-P., and Vissenberg, K. (2013). Microfilament Analyzer identifies actin network organizations in epidermal cells of Arabidopsis thaliana roots. *Plant Signal Behav*, 8(7):e24821.
- [36] Jeong, H., Tombor, B., Albert, R., Oltvai, Z., and Barabási, A.-L. (2000). The large-scale organization of metabolic networks. *Nature*, 407:651–654.
- [37] Jones, E., Oliphant, T., and Peterson, P. (2001). SciPy: open source scientific tools for Python.
- [38] Jordano, P., Bascompte, J., and Olesen, J. M. (2003). Invariant properties in coevolutionary networks of plant-animal interactions. *Ecol Lett*, 6(1):69–81.
- [39] Katifori, E., Szöllősi, G. J., and Magnasco, M. O. (2010). Damage and fluctuations induce loops in optimal transport networks. *Phys Rev Lett*, 104(4):048704.
- [40] Koch, C. and Laurent, G. (1999). Complexity and the nervous system. *Int S Techn Pol Inn*, 284(5411):96–98.
- [41] Le, J., Vandebussche, F., De Cnodder, T., Van Der Straeten, D., and Verbelen, J.-P. (2005). Cell elongation and microtubule behavior in the arabidopsis hypocotyl: responses to ethylene and auxin. *J Plant Growth Regul*, 24(3):166–178.
- [42] Lee, M. C. S., Miller, E. A., Goldberg, J., Orci, L., and Schekman, R. (2004). Bi-directional protein transport between the er and golgi. *Annu Rev Cell Dev Biol*, 20:87–123.
- [43] Lieleg, O., Claessens, M., Heussinger, C., Frey, E., and Bausch, A. (2007). Mechanics of bundled semiflexible polymer networks. *Phys Rev Lett*, 99(8):088102.
- [44] Lindeboom, J. J., Nakamura, M., Hibbel, A., Shundyak, K., Gutierrez, R., Ketelaar, T., Emons, A. M. C., Mulder, B. M., Kirik, V., and Ehrhardt, D. W. (2013). A mechanism for reorientation of cortical microtubule arrays driven by microtubule severing. *Int S Techn Pol Inn*, 342(6163):1245533.
- [45] Louf, R., Jensen, P., and Barthélemy, M. (2013). Emergence of hierarchy in cost-driven growth of spatial networks. *Proc Natl Acad Sci*, 110(22):8824–8829.
- [46] MacKintosh, F., Käs, J., and Janmey, P. (1995). Elasticity of semiflexible biopolymer networks. *Phys Rev Lett*, 75(24):4425.
- [47] Neri, I., Kern, N., and Parmeggiani, A. (2013). Modeling cytoskeletal traffic: an interplay between passive diffusion and active transport. *Phys Rev Lett*, 110(9):098102.

- [48] Newman, M. (2009). *Networks: an introduction*, volume 1. Oxford Univ Press.
- [49] Oliphant, T. E. (2006). *A Guide to NumPy*, volume 1. Trelgol Publishing USA.
- [50] Paradez, A., Wright, A., and Ehrhardt, D. W. (2006). Microtubule cortical array organization and plant cell morphogenesis. *Curr Opin Plant Biol*, 9(6):571–578.
- [51] Paradez, A. R., Somerville, C. R., and Ehrhardt, D. W. (2006). Visualization of cellulose synthase demonstrates functional association with microtubules. *Int S Techn Pol Inn*, 312(5779):1491–1495.
- [52] Rogers, S. L. and Gelfand, V. I. (2000). Membrane trafficking, organelle transport, and the cytoskeleton. *Curr Opin Cell Biol*, 12(1):57–62.
- [53] Sambade, A., Pratap, A., Buschmann, H., Morris, R. J., and Lloyd, C. (2012). The influence of light on microtubule dynamics and alignment in the Arabidopsis hypocotyl. *Plant Cell Online*, 24(1):192–201.
- [54] Sampathkumar, A., Gutierrez, R., McFarlane, H. E., Bringmann, M., Lindeboom, J., Emons, A.-M., Samuels, L., Ketelaar, T., Ehrhardt, D. W., and Persson, S. (2013). Patterning and lifetime of plasma membrane-localized cellulose synthase is dependent on actin organization in Arabidopsis interphase cells. *Plant Physiol*, 162(2):675–688.
- [55] Sampathkumar, A., Lindeboom, J. J., Debolt, S., Gutierrez, R., Ehrhardt, D. W., Ketelaar, T., and Persson, S. (2011). Live cell imaging reveals structural associations between the actin and microtubule cytoskeleton in Arabidopsis. *Plant Cell*, 23(6):2302–2313.
- [56] Schindelin, J., Arganda-Carreras, I., Frise, E., Kaynig, V., Longair, M., Pietzsch, T., Preibisch, S., Rueden, C., Saalfeld, S., Schmid, B., et al. (2012). Fiji: an open-source platform for biological-image analysis. *Nat Methods*, 9(7):676–682.
- [57] Shafrir, Y., ben Avraham, D., and Forgacs, G. (2000). Trafficking and signaling through the cytoskeleton: a specific mechanism. *Sci Signal*, 113(15):2747.
- [58] Shafrir, Y. and Forgacs, G. (2002). Mechanotransduction through the cytoskeleton. *J Cell Physiol*, 282(3):C479–C486.
- [59] Shimmen, T. and Yokota, E. (2004). Cytoplasmic streaming in plants. *Curr Opin Cell Biol*, 16(1):68–72.
- [60] Staiger, C. J., Sheahan, M. B., Khurana, P., Wang, X., McCurdy, D. W., and Blanchoin, L. (2009). Actin filament dynamics are dominated by rapid growth and severing activity in the Arabidopsis cortical array. *J Cell Biol*, 184(2):269–280.
- [61] Sternberg, S. R. (1983). Biomedical image processing. *Computer*, 16(1):22–34.
- [62] Sun, J., Boyd, S., Xiao, L., and Diaconis, P. (2006). The fastest mixing markov process on a graph and a connection to a maximum variance unfolding problem. *Siam Rev*, 48(4):681–699.
- [63] Szymanski, D. B. (2009). Plant cells taking shape: new insights into cytoplasmic control. *Curr Opin Plant Biol*, 12(6):735–744.
- [64] Tindemans, S. H., Hawkins, R. J., and Mulder, B. M. (2010). Survival of the aligned: ordering of the plant cortical microtubule array. *Phys Rev Lett*, 104(5):058103.
- [65] Van Rossum, G. and Drake Jr, F. L. (2006). *The Python Language Reference Manual*, volume 1. Network Theory Ltd, Godalming, UK.
- [66] Wagner, B., Tharman, R., Haase, I., Fischer, M., and Bausch, A. (2006). Cytoskeletal polymer networks: the molecular structure of cross-linkers determines macroscopic properties. *Proc Natl Acad Sci*, 103(38):13974–13978.
- [67] Waller, F. and Nick, P. (1997). Response of actin microfilaments during phytochrome-controlled growth of maize seedlings. *Protoplasma*, 200(3-4):154–162.
- [68] Wasteneys, G. O. (2000). The cytoskeleton and growth polarity. *Curr Opin Plant Biol*, 3(6):503–511.
- [69] Wasteneys, G. O. and Ambrose, J. C. (2009). Spatial organization of plant cortical microtubules: close encounters of the 2D kind. *Trends Cell Biol*, 19(2):62–71.
- [70] West, D. B. et al. (2001). *Introduction to graph theory*, volume 2. Prentice Hall Englewood Cliffs.
- [71] West, G. B., Brown, J. H., and Enquist, B. J. (1997). A general model for the origin of allometric scaling laws in biology. *Int S Techn Pol Inn*, 276(5309):122–126.
- [72] West, G. B., Brown, J. H., and Enquist, B. J. (1999). A general model for the structure and allometry of plant vascular systems. *Nature*, 400(6745):664–667.
- [73] Williams, S. R. and Stuart, G. J. (2000). Action potential backpropagation and somato-dendritic distribution of ion channels in thalamocortical neurons. *J Neurosci*, 20(4):1307–1317.
- [74] Wymer, C. and Lloyd, C. (1996). Dynamic microtubules: implications for cell wall patterns. *Trends Plant Sci*, 1(7):222–228.
- [75] Yarmola, E. G., Somasundaram, T., Boring, T. A., Spector, I., and Bubb, M. R. (2000). Actin-latrunculin A structure and function differential modulation of actin-binding protein function by latrunculin A. *J Biol Chem*, 275(36):28120–28127.
- [76] Ziemann, F., Rädler, J., and Sackmann, E. (1994). Local measurements of viscoelastic moduli of entangled actin networks using an oscillating magnetic bead microrheometer. *Biophys J*, 66(6):2210–2216.
- [77] Zumdieck, A., Cosentino Lagomarsino, M., Tanase, C., Kruse, K., Mulder, B., Dogterom, M., and Jülicher, F. (2005). Continuum description of the cytoskeleton: ring formation in the cell cortex. *Phys Rev Lett*, 95(25):258103.

## Appendix A1: Experimental setup

Here, we describe the experimental setup for recording the cytoskeleton of growing plant cells. Dual-labeled *Arabidopsis thaliana* Columbia-0 seedlings were previously described in [55]. The seedlings were surface sterilized (ethanol), stratified for 2 days at 4°C and germinated on MS agar plates (1X Murashige and Skoog salts, 8 g/L agar, 1X B5 vitamins, and 10.8 g/L sugar). All plants were grown in the dark on vertical plates at 21.8°C for 3 days. For treatment with Latrunculin B, seedlings were floated on distilled water containing 150  $\mu$ M Latrunculin B and a set of control seedlings on pure water in 6-well plates. The seedlings were incubated in the dark with gentle shaking for 4 hours before imaging. For light treatments, a plate of dark-grown seedlings was exposed to light (150  $\mu$ E m<sup>-2</sup> s<sup>-1</sup> PAR) for 4 hours while a control plate was kept in the dark, both plates being maintained in a vertical orientation. To study the effect of Latrunculin B, 5 control and 5 treated cells were imaged. For the analysis of the effect of light on the cytoskeleton, 35 control and 26 treated cells were imaged. To fix the seedlings and to avoid mechanical damage, they were mounted between a cover glass and a 1 mm thick 1% agar pad affixed on a circular cover slip. A detailed description of the microscopy setup is given in ref. [55]. Typical exposure times were 400 ms for GFP and 300 ms for mCherry with a time interval of 2 s between subsequent actin and microtubule images, respectively. The cells were recorded for at least 4 min. Only seedlings expressing both fluorescent markers were used for further analyses.

## Appendix A2: Network reconstruction procedure, different grid topologies and null models

We now explain our method for reconstructing a (edge-weighted, undirected) network from the confocal image series of actin filaments or microtubules and present various extensions and null models. We preprocessed the recorded image series using Fiji [56]: First, the drift of the seedlings under the microscope was corrected using a stack registration algorithm [3]. Here, the microtubule images were registered first because they are less dynamic and easier for the program to align. The more dynamic actin filaments were then subjected imagewise to the same transformations. Second, the image series were rotated so that the shoot apical direction of the cell pointed upwards. The region of interest, i.e., the interior of the cell, was cropped manually and identically for the corresponding actin and microtubule frames. Third, the background noise was reduced by applying a rolling ball background subtraction [61], with a ball radius of 50 pixels. The noisy background signal arises largely from fluorescent monomeric actin/tubulin in the cytosol which is not incorporated in filaments and, hence, was filtered out in the present study. Finally, photobleaching was compensated by rescaling all images' mean intensities to one.

From these preprocessed images we obtained the cytoskeletal components as complex networks through a two-step procedure as described in the main text (cf. section "Reconstruction of complex networks from cytoskeletal images"). These steps and all statistical analyses were performed using Python [65]. We chose an equidistant rectangular grid with a spacing of 10 pixels and the standard deviation of the Gaussian convolutions kernels was 4 pixels in x- and y-direction, unless stated otherwise. An extension of our framework is the three-dimensional network that may be easily reconstructed from three-dimensional confocal microscope image series (Fig. 1G). First, a network was reconstructed for each z-slice as for the two-dimensional case. Then, for a rectangular grid, the networks of neighboring z-slices were connected by creating a link between nodes with the same x-y-coordinates. The weights of these links were computed by creating Gaussian convolution kernels (pointsymmetric, with the same width as for the edges, i.e., 4 pixels) for its nodes, multiplying them with the two respective z-slices and averaging over the sum of the resultant images. The three-dimensional network reconstruction captures cytoskeletal filaments which leave the cortical plane and may be analyzed using the same network-based methods as for the two-dimensional networks.

To ensure that our findings (e.g., on the transport efficiency of the cytoskeletal network architecture that displays short APLs; see section "Accessibility and robustness of cytoskeletal networks"), are valid not only for rectangular grids, we tested other grid types. We reconstructed the cytoskeletal actin network of the same cell based on two-dimensional rectangular, triangular, and hexagonal grids with spacings of 10 and 20 pixels and a three-dimensional grid with a uniform spacing of 20 pixels (Fig. A1A). For these networks, we compared the APLs to an ensemble of null model networks obtained by edge-shuffling. In all chosen grid types, the APL of the observed network is significantly shorter than expected from the respective null model (Fig. A1B; one-sample two-sided *t*-test: all *p*-values < 0.05). Hence, the short APLs of the cytoskeleton are a non-random and biologically relevant feature which does not arise as an artifact of the imposed grid type. As network properties are often dependent on each other, the findings from the comparative analysis suggest that a significant change of other network properties compared to their null model values is largely independent of the underlying grid type, as long as the grid is not too dense, covers the cell too inhomogeneously (e.g., random geometric graphs), or has non-local, long-range links (e.g., scale-free graphs).

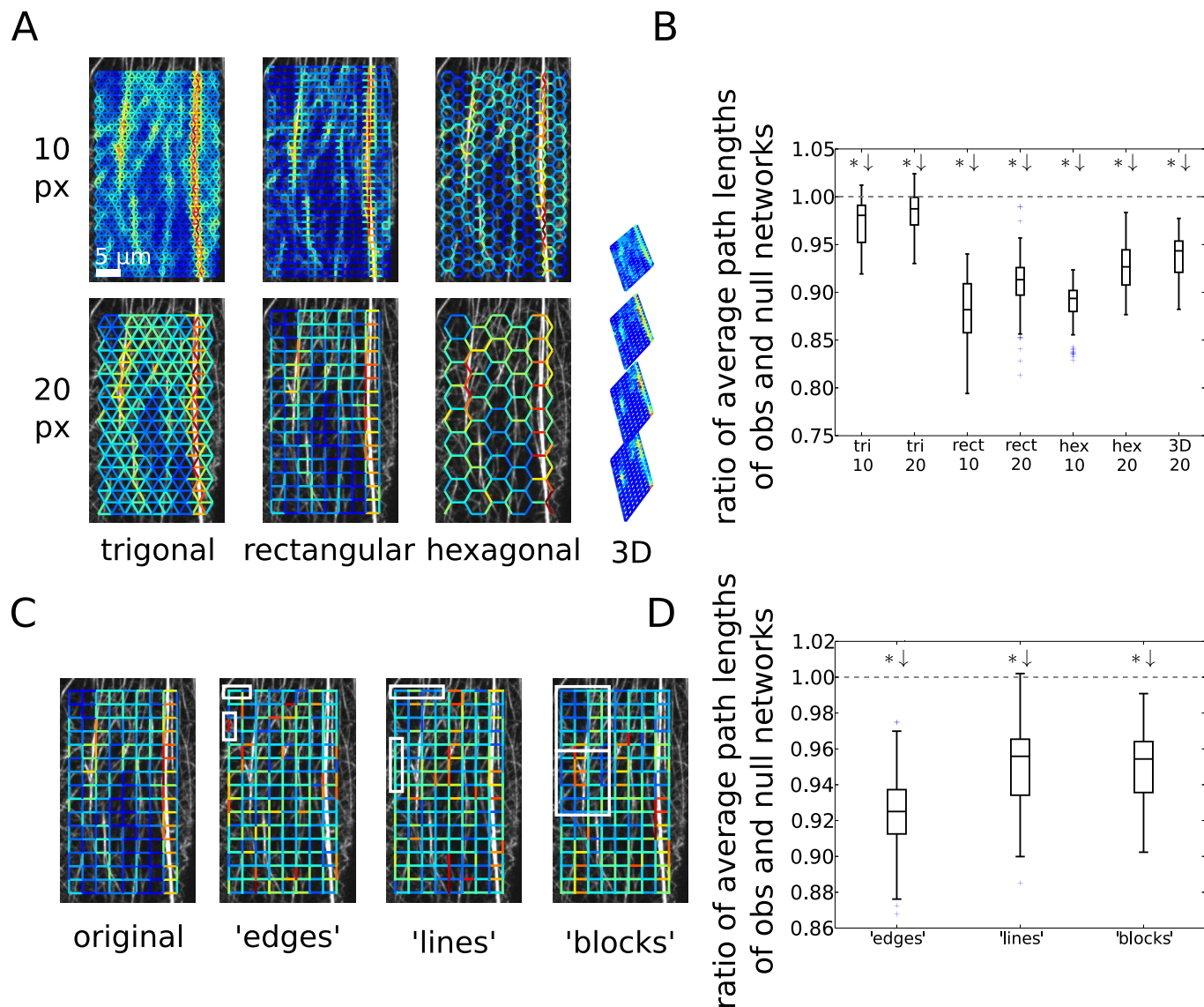


**Figure A1. Extensions of the network reconstruction framework and different null models.** (A) Reconstructions of the actin cytoskeleton of the same cell using different sizes (grid spacings of 10 and 20 pixels) of triangular, rectangular, and hexagonal grids, and a three-dimensional grid with 20 pixel-spacings. (B) All studied grid types exhibit smaller average path lengths than their respective null model networks. (C) Different null models for the reconstructed network were obtained by shuffling all edge weights, by shuffling connected vertical and horizontal lines, and by rearranging blocks of varying size and shuffling the remaining edge weights, respectively. White rectangles exemplify sections of the cytoskeletal network that were shuffled. (D) All proposed null models yield values below one for ratio of the average path lengths of observed and null model networks, suggesting a non-random and efficient organization of the cytoskeletal network.

Judging the biological relevance of a network property's value requires a meaningful comparison since its value depends on the normalization of the image and is therefore arbitrary. The simplest reference is given by the values of the respective network property which are obtained for null model networks with shuffled edge weights (Fig. A1C, "edges"). Such networks preserve both the node positions and the distribution of edge weights and thus the total amount of cytoskeletal components in the cell. By comparing the value of a given network property of a reconstructed cytoskeletal network against those of an ensemble of edge-shuffled null model networks, we were able to assess whether a random distribution of cytoskeletal material in the cell results in the same cytoskeletal properties as realized in the observed cell, see section "Accessibility and robustness of cytoskeletal networks". For example, for the APL, the ratio of observed and null model values falls significantly below one (Fig. A1D, "edges"; one-sample two-sided  $t$ -test:  $p$ -value  $< 0.05$ ).

We also investigated two alternative null models to strengthen the assessment of the biological relevance of different network properties. Like the first null model, these, too, preserve the positions of the nodes of the network and the distribution of edge weights in the network. In addition, they leave more of the local cytoskeletal structure intact. While in the first null model, edge weights were shuffled irrespective of the edges to which they were assigned, we now cut all edges forming connected horizontal or vertical lines into several equal sections, respectively, which were in turn shuffled (Fig. A1C, “lines”; here, horizontal lines are divided into three and vertical lines in four sections). This method better preserves potential strongly weighted paths and hence the filamentous structures of the cytoskeleton. As for the “edge” null model, this “line” null model exhibits longer APLs than the observed network (Fig. A1D, “lines”; one-sample two-sided  $t$ -test:  $p$ -value  $< 0.05$ ). Clearly, the focus on horizontal or vertical lines imposes a restriction to the orientation of potential filaments. To circumvent this limitation, we analyzed a third null model in which connected, non-overlapping blocks of nodes were chosen. The subgraphs formed by these blocks were shuffled as well as the remaining edge weights that were not part of any subgraph (Fig. A1C, “blocks”; here, the network is composed into three times four blocks). This “block” null model also exhibits longer APLs than its biological counterpart (Fig. A1D, “blocks”; one-sample two-sided  $t$ -test:  $p$ -value  $< 0.05$ ). More sophisticated null models may be proposed. However, the investigation of three different null models that capture the amount of cytoskeletal components in the cell and their filamentous structure provided consistent results on the non-randomness of various cytoskeletal network properties. Using the simple null model was, therefore, considered reliable for assessing the biological relevance of the studied network properties (see section “Accessibility and robustness of cytoskeletal networks”).

### Appendix A3: Network properties used for quantifying the cytoskeletal organization

In the manuscript, we represent the cytoskeleton as a weighted, undirected network and quantify its structure via a number of seminal network properties. Here, we explain the employed properties in more detail and provide careful interpretations of how they relate to the structural (and potentially: functional) features of the cytoskeleton. In the following, we consider a weighted, undirected network  $G = (\mathcal{N}, \mathcal{E})$  with a set  $\mathcal{N}$  of  $N = |\mathcal{N}|$  nodes, a set  $\mathcal{E}$  of  $E = |\mathcal{E}|$  undirected edges  $e = (n, m) \equiv (m, n) \in \mathcal{E}$  and  $m, n \in \mathcal{N}$  with weights  $w_e$ .

**Degree distribution:** The degree  $d_n$  of a node  $n \in \mathcal{N}$  is given by the sum of its edge weights  $w_e$ , i.e.,

$$d_n = \sum_{\substack{e \in \mathcal{E} \\ n \in e}} w_e \quad (\text{A31})$$

(cf. Fig. A2A for the degree of a node of the network in panel E; color-coded node degrees in Figs. A2E-H). Since the edge weights reflect the intensity of cytoskeletal structures close to the respective edges, the node degrees reflect the cytoskeletal intensities in the vicinity of the respective nodes. Therefore, the standard deviation of the degree distribution (SDD) captures the spatial heterogeneity of the distribution of intensities in the underlying cytoskeleton images,

$$\text{SDD} = \left( \left( N^{-1} \sum_{n=1}^N d_n^2 \right) - \left( N^{-1} \sum_{n=1}^N d_n \right)^2 \right)^{-1/2}. \quad (\text{A32})$$

In particular, the SDD does not measure the heterogeneity in filament thicknesses or numbers but a combination thereof. Comparing Figs. A2E and G, we find that the SDD of the former network is smaller, indicating a more homogeneous spatial distribution of the cytoskeleton in agreement with the visual impression.

**Connected components:** By construction, all edges in the reconstructed networks are strictly positive (because the Gaussian convolution kernels are strictly positive and have infinite support and the image intensity is greater than zero somewhere in the image) and, hence, all their nodes are connected. However, when removing edges, e.g., with small weights by arguing that they do not permit transport of cargo, the network may disconnect and split into several connected components (cf. Fig. A2B for the thresholded version of the network in panel F). The components are called trivial if they consist of a single node only, and non-trivial otherwise. For simplicity, we use the 50th percentile when thresholding the edge weights throughout the manuscript but our findings remain qualitatively unchanged when different, reasonable thresholds are

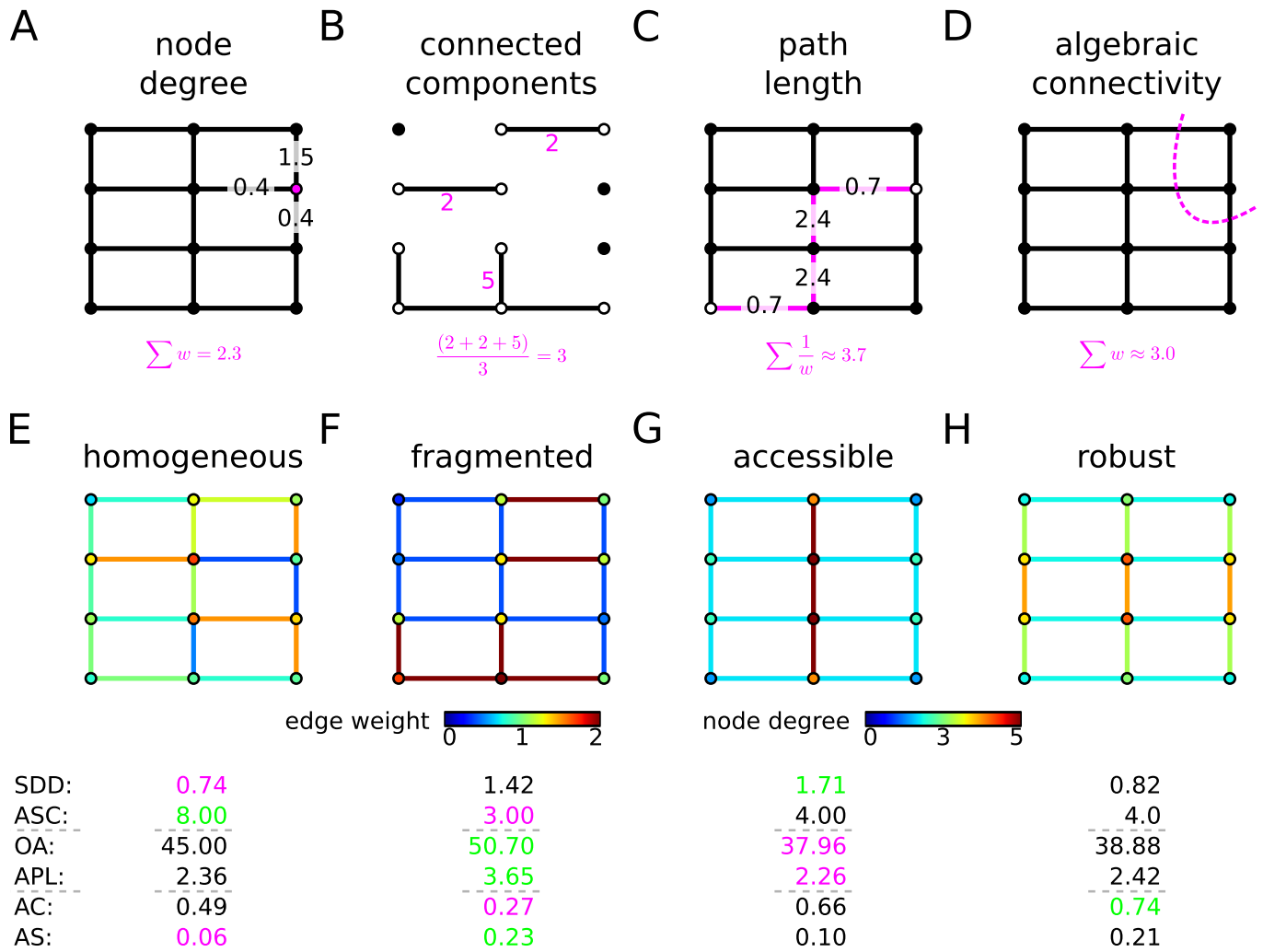


Figure A2. **Explanations of different network properties and exemplary networks with different structural and functional characteristics.** Panels (A)-(D) display schematic illustrations of different network properties. Panels (E)-(H) show typical paradigmatic networks with color-coded edge weights and node degrees. **(A)** The degree of a node is given by the sum of its edge weights, cf. color-coding in panel (E). **(B)** When removing edges with weights below the 50th percentile from the network in panel (F), the network decomposes into trivial components with just a single node (black circles) and several bigger, non-trivial components (white circles). **(C)** The shortest path length between two nodes is given by a sequence of edges whose sum of inverse weights is minimal, cf. network in panel (G). **(D)** The algebraic connectivity relates to the minimum sum of the weights of edges that need to be removed to disconnect the network, cf. network in panel (H). **(E)** The network exhibits a small standard deviation of the degree distribution (SDD), has a large average size of the connected components (ASC) after thresholding, and a small assortativity (AS). **(F)** The network has a small ASC, its overall angle (OA) indicates a horizontal orientation ( $OA > 45^\circ$ ), it displays a large average path length (APL), a small algebraic connectivity (AC), and a large assortativity. **(G)** The network has a high SDD, displays a vertical OA ( $OA < 45^\circ$ ), and a small APL. **(H)** The network was obtained by maximizing the AC for a fixed sum of weights (cf. discussion of Fig. 4) and, accordingly, displays a high AC.

chosen. The average number of nodes per non-trivial connected component (ASC) is a measure for the fragmentation of the network.

$$ASC = C^{-1} \sum_{c=1}^C N_c, \quad (\text{A33})$$

where  $\mathcal{C}$  is the set of  $C = |\mathcal{C}|$  non-trivial components and  $N_c$  is the number of nodes in component  $c \in \mathcal{C}$ . Comparing Figs. A2E and F, we find that the ASC is smaller in the latter which clearly exhibits several small, densely connected fragments separated by weak connections.



**Overall angle:** As our network representation does not resolve individual filaments, we can not evaluate their orientations individually. However, our approach allows to infer an overall angle (OA) for the orientation of the cytoskeletal structures as a whole. The OA is given by Eq. (A45) and its derivation is explained in ESM4. Two networks with different OA are shown in Figs. A2F and G with overall horizontal ( $OA > 45^\circ$ ) and vertical ( $OA < 45^\circ$ ) orientations, respectively, as confirmed visually.

**Average path length:** A path  $\mathcal{P}$  between two nodes is a sequence of edges connecting the nodes. A shortest path is a path that minimizes its sum of edge lengths (cf. Fig. A2C for a shortest path in the network in panel G). Here, for simplicity, we take the length of an edge to be the inverse of its weight. This choice takes into account that parts of the cytoskeleton that yield strong edge weights potentially allow faster/more transport as reflected by small edge lengths.

$$\text{APL} = 2^{-1} N^{-1} (N - 1)^{-1} \sum_{n=1}^N \sum_{\substack{m=1 \\ m > n}}^N \min_{\mathcal{P} \in \mathcal{P}_{n,m}} \sum_{e \in \mathcal{P}} w_e^{-1}, \quad (\text{A34})$$

where  $\mathcal{P}_{n,m}$  is the set of all paths from node  $n$  to  $m$  and  $w_e^{-1}$  is the length of the edge  $e \in P \in \mathcal{P}_{n,m}$ . As explained in the discussion of Fig. 3 in the main text, highway-like structures may yield small average path lengths (APL) as they act as short cuts between distant parts of the network. Such a highway-like structure is given by the network in Fig. A2G which, accordingly, displays a smaller APL than, e.g., the easily-fragmented network in panel F.

**Algebraic connectivity:** The algebraic connectivity is the second smallest eigenvalue

$$\text{AC} \equiv \lambda_2 \quad (\text{A35})$$

of the graph Laplacian  $L$ ,

$$L_{n,m} = \begin{cases} d_n & \text{if } n = m \\ -w_{(n,m)} & \text{if } (m,n) \in \mathcal{E} \\ 0 & \text{otherwise,} \end{cases} \quad (\text{A36})$$

with  $n, m \in \mathcal{N}$ . By construction of  $L$ , its smallest eigenvalue  $\lambda_1 = 0$  and the number of zero eigenvalues provides the number of connected components in the graph (cf. e.g. [48]). As our reconstructed networks are always connected (see the discussion of the connected components above) they yield  $\lambda_2 \equiv \text{AC} > 0$ . The magnitude of the AC is commonly interpreted as a measure for how well-knit the network is, which is related to the minimum sum of the weights of edges that need to be removed in order to disconnect the network (cf. Fig. A2D). We solved a semi-definite optimization problem described in the discussion of Fig. 4 to construct a network with a fixed sum of edge weights that maximizes the AC. This network is shown in Fig. A2H and its AC is larger than, e.g., that of the easily-fragmented network in panel F. We note that small APL and large AC favor different types of networks (cf. Figs. A2G and H). This may be explained as follows: In the computation of the APL for each shortest path only one edge may be used at a time. In contrast, the AC is related to cuts (i.e., the removal of sets of edges) that disconnect the network and hence affect multiple edges. Thus, the APL and the AC are independent network properties that provide insights into different potential, transport-related functions of the cytoskeleton.

**Assortativity:** The assortativity denotes the correlation of the degrees of neighboring nodes

$$\text{AS} = \frac{1}{2E} \sum_{n=1}^N \sum_{m=1}^N \left( w_{(n,m)} - \frac{d_n d_m}{2E} \right) d_n d_m. \quad (\text{A37})$$

Similar to the SDD (see above) the AS captures the spatial heterogeneity of the cytoskeletal components but contains additional information about its spatial distribution: The AS is high if nodes with high (low) degrees are also connected to nodes with similar degrees, hence detecting regions of spatially clustered cytoskeletal structures. For instance, Fig. A2E displays a network with low AS because there are no regions of nodes of high or low degree clustered together, while the network in panel F shows high AS values that reflect regions of high and low node degrees, respectively.

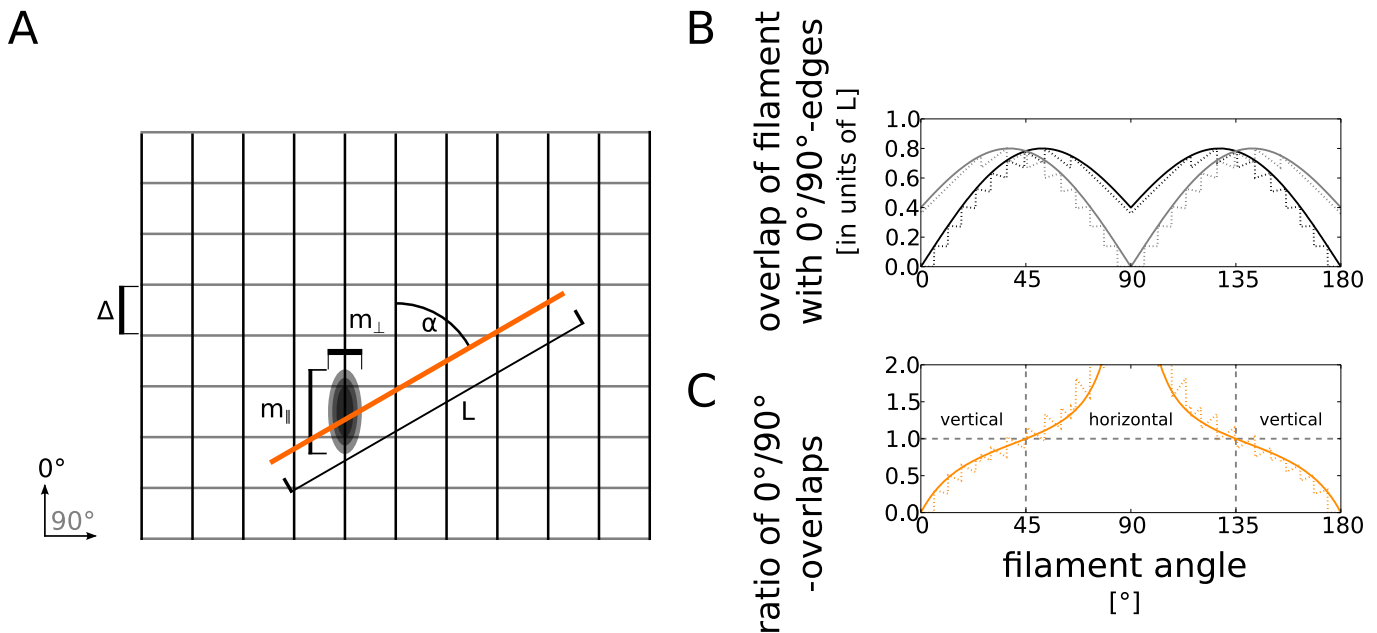


Figure A3. **Inferring orientation of filament from network structure.** (A) Schematic filament of length  $L$  at an angle  $\alpha$ , placed on a rectangular grid with spacing  $\Delta$ , vertical ( $0^\circ$ , black), and horizontal edges ( $90^\circ$ , gray). The shape of the edges' convolution kernels determines the contribution of the filament to each edge, with the two extremes  $m_{\parallel}$  and  $m_{\perp}$  for parallel and perpendicular orientation of the filament with respect to the edge. (B) Contribution of filaments ( $L = 1000$ , solid lines;  $L = 10$ , dotted lines) to edges of different orientation ( $0^\circ$ , black;  $90^\circ$ , gray) for varying angles  $\alpha$ . By including that filaments cross only integer numbers of edges, we obtain curves that are strongly discontinuous for short filaments and become less discontinuous for longer filaments. (C) The ratio of filament overlaps  $r$  with  $0^\circ$ - and  $90^\circ$ -edges determines the filament angle ( $L = 1000$ , solid line;  $L = 10$ , dotted line), with  $r < 1$  and  $r > 1$  corresponding to a vertical and horizontal orientation, respectively.

#### Appendix A4: Method for determining angles and filament orientations from network structure

We now present a method to evaluate the orientation of AFs and MTs by exploiting their network structures. Starting from a given grid (Fig. A3A), we placed a stiff rod of length  $L$  that is rotated by an angle  $\alpha$  and computed its contribution to the weight of edges with an orientation of angle  $\gamma$ . Assuming a regular grid in which edges with angle  $\gamma$  are distributed with uniform distances  $\Delta$ , we calculated the number  $n_{\gamma}$  of crossed  $\gamma$ -edges,

$$n_{\gamma} = \Delta^{-1} L |\sin(\alpha - \gamma)|. \quad (\text{A41})$$

The overlap  $m$  of the rod and a  $\gamma$ -edge was computed via the convolution kernel of that edge (see section “Network reconstruction procedure, different grid topologies and null models”) and was approximated as

$$m_{\gamma} = m_{\perp} + (m_{\parallel} - m_{\perp}) |\cos(\alpha - \gamma)|, \quad (\text{A42})$$

where  $m_{\perp}$  and  $m_{\parallel}$  are the contributions of the rod to the edge when they are perpendicular or parallel to each other. The total contribution of the rod to all  $\gamma$ -edges is (Eqs. (A41) and (A42))

$$w_{\gamma} = n_{\gamma} m_{\gamma} = \Delta^{-1} L |\sin(\alpha - \gamma)| [m_{\perp} + (m_{\parallel} - m_{\perp}) |\cos(\alpha - \gamma)|]. \quad (\text{A43})$$

Furthermore, we may include that only integer numbers of edges may be crossed by a filament. Then,  $L \sin$  in Eq. (A43) is replaced by  $\lfloor L \sin \rfloor$  and the contribution of a filament of finite length becomes discontinuous and approaches the continuous curve for long filaments (Fig. A3B). For simplicity, we considered small grid spacings or long filaments and work with Eq. (A43) directly. Each cytoskeleton fluorescence image contains many filaments and their lengths and

orientations can not be inferred uniquely from the distribution of edge weights. Because  $m_{\perp}$  and  $m_{\parallel}$  are determined by the convolution kernels, the ratio of the weights of two edge types with different orientations  $\gamma$  and  $\gamma'$  yields an equation for  $\alpha$ ,

$$\frac{w_{\gamma}}{w_{\gamma'}} = \frac{|\sin(\alpha - \gamma)| [m_{\perp} + (m_{\parallel} - m_{\perp}) |\cos(\alpha - \gamma)|]}{|\sin(\alpha - \gamma')| [m_{\perp} + (m_{\parallel} - m_{\perp}) |\cos(\alpha - \gamma')|]} =: r, \quad (\text{A44})$$

where  $\alpha$  may be interpreted as the overall orientation of the cytoskeletal filaments (Fig. A3C). For  $\gamma = 0^{\circ}$  and  $\gamma' = 90^{\circ}$ , Eq. (A44) yields

$$\alpha = \arctan \left( \frac{m_{\perp} + r(m_{\parallel} - m_{\perp})}{m_{\perp} r + (m_{\parallel} - m_{\perp})} \right). \quad (\text{A45})$$

In our analysis, we refer to  $\alpha \in [0^{\circ}, 45^{\circ})$  and  $\alpha \in (45^{\circ}, 90^{\circ}]$  as an overall vertical and horizontal orientation, respectively. See section ‘‘The reconstructed networks capture biologically relevant features of the actin and microtubule cytoskeletal components’’ for results on the orientation of the cytoskeletal components under different conditions.

#### Appendix A5: Reconstruction and analysis of the German autobahn network

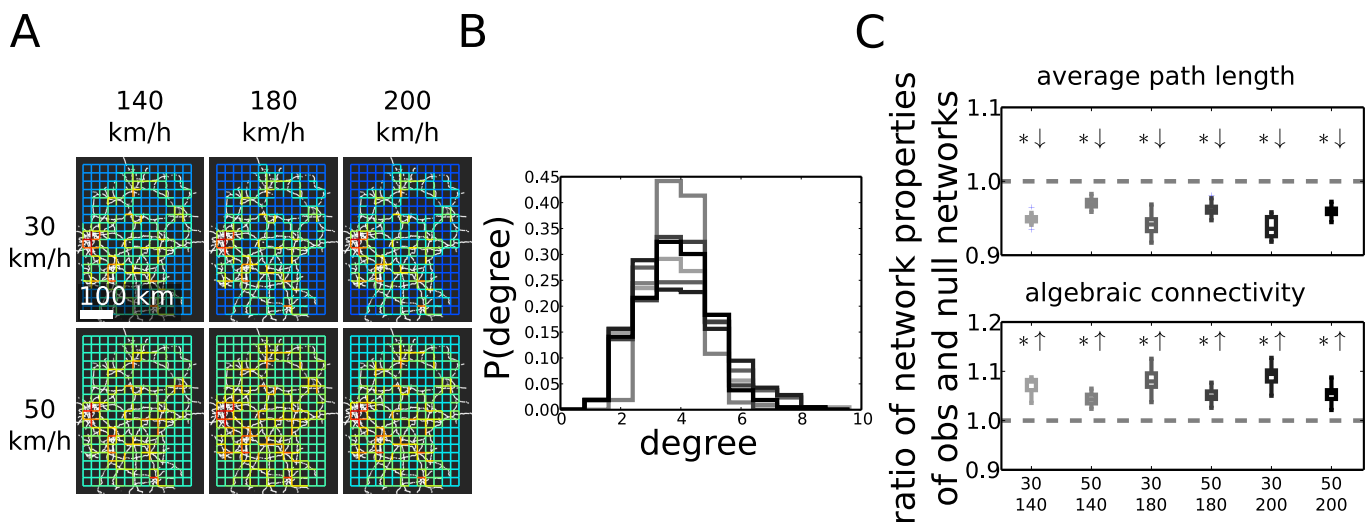


Figure A4. **The efficiency of the autobahn network is pertained for different choices of speed limits.** (A) Reconstructed autobahn networks with different maximum high speed limits (140, 180, and 200 km/h) and different off-highway speed limits (30 and 50 km/h). (B) The degree distributions of the autobahn networks with the different speed limits given in (A) (from light gray to black) are unimodal and centered around their means (excess kurtosis  $> 0$ ). (C) The ratios of average path lengths and algebraic connectivities of observed and null model networks are well below and above one, respectively, for all autobahn networks with speed limits described in (A).

Here, we describe the data and the procedure used for reconstructing the German autobahn as a network for a comparison with the plant cytoskeleton. Further, we present two examples of networks with different structural and transport-related properties.

An OpenStreetMap (© OpenStreetMap contributors; map data available under the Open Database License (ODbL)) data set of Germany was downloaded (<http://download.geofabrik.de/europe/germany.html>; © Geofabrik GmbH Karlsruhe), converted to .osm for faster filtering (<http://wiki.openstreetmap.org/wiki/Osmconvert>), and filtered for objects of type ‘‘highway=motorway’’ (<http://wiki.openstreetmap.org/wiki/Osmfilter>). The remaining motorways were parsed in Python. Speed limits

were taken into account for better analogy with the cytoskeleton that exhibits thinner and thicker bundles that were argued in the main text to allow different net transportation speeds. Because some sections of the autobahn were assigned no speed limits (either because of lacking data or the absence of a speed limit) and to incorporate transportation outside of the autobahn, we chose different settings to ensure the robustness of our findings: Missing autobahn speed limits were set to 140, 180, and 200 km/h and the speed limit in the rest of Germany was set to 30 and 50 km/h, respectively (Fig. A4A).

The results for speed limits of 200 km/h and 50 km/h (Fig. 4; section “The cytoskeleton and the German autobahn exhibit similar network properties”) demonstrate that the autobahn network displays a unimodal degree distribution that peaks around its mean and that it exhibits significantly shorter path length and a significantly higher AC than the null model networks. The same holds true for all considered speed limits (Fig. A4B and C; one-sample two-sided  $t$ -test: all  $p$ -values  $< 0.05$ ). Hence, the findings on the efficiency of the autobahn networks are robust against moderate changes of the speed limits.